Observation of Cross-Link Density Dispersion in Sulfur Donor-Vulcanized Polybutadiene Using NMR Imaging

S. R. Smith and J. L. Koenig*

Department of Macromolecular Science, Case Western Reserve University, Cleveland, Ohio 44106

Received June 14, 1990; Revised Manuscript Received December 5, 1990

ABSTRACT: Proton NMR imaging techniques have been applied to the investigation of two-dimensional structure in TMTD-vulcanized *cis*-polybutadiene. Unfilled PB samples of different cross-link densities were swollen with deuterated solvent and directly imaged, using single and multiple spin-echo NMR imaging (NMRI) pulse sequences. The resulting T_2-weighted and T_2-resolved images display a variety of structural detail. Major structural voids, compression- and reaction-induced gradients of chain segment mobility, and general spatial inhomogeneity in the cross-link density of these samples have been observed. A simple analytical model has been applied to interpret changes in the distribution of T_2 values with increasing cure time. The results of this work form the basis for quantitative assessment of spatial variations in the cross-link density of PB from T_2-resolved images of the material.

Introduction

Since the advent of high-resolution solid-state NMR methods in the early 1970s, NMR spectroscopy has been extensively used to investigate the molecular structure and dynamics of cross-linked polymer systems.[1-3] Cross-linked elastomers have received particularly wide attention for a variety of reasons. Among these are the practical utility of objects made from such materials, as well as the ability of many systems to be chemically tailored to form model cross-linked networks. Analytical interest in the study of cross-linked elastomers has been maintained by the amenability of this class of flexible polymers to many of the specialized NMR techniques originally designed to study materials in solution. Moreover, dating from Flory's initial contributioins to the understanding of rubber elasticity in the 1940s, an extensive body of theory is available to support the design and interpretation of experimental investigations in this area.[4-6]

Paralleling developments in the field of one-dimensional NMR spectroscopy for in situ analysis of solid-state materials has been the growth of NMR imaging (NMRI) as a tool for two- and three-dimensional resolution of structure.[7-20] The motivation for use of NMRI in application to cross-linked polymer systems derives from the dependence of these materials' mechanical properties not simply on bulk parameters, such as physical and chemical cross-link densities, volume fraction of filler, or concentration of voids or defects, but on the three-dimensional spatial distribution of these structures throughout the polymer network. Cross-linked elastomers are especially well-suited candidates for NMR imaging studies, due both to their high segmental mobility at ambient temperatures and to their large extensibility on being swollen in appropriate solvents. Given the magnetic field gradient strengths available in current commercial NMR imaging probes, the ability to swell elastomers to several times their original dimensions enables resolution of morphologically well-defined features, such as voids, which are dimensionally on the order of microns in the precursor unswollen materials. In the more general case, detailed three-dimensional structural analysis of elastomer samples is made possible by observation of the spatial distributions of their proton spin-spin and spin-lattice parameters, T_1 and T_2. This statement assumes that variations in T_1 and T_2 derive from similar variations in the extent of motion of elastomer chain segments, reflecting their positions relative to sites of decreased mobility, such as cross-links or filler particles, or to sites of increased mobility, such as microscopic voids or other defects.

The present study is concerned with investigating the structure of samples of high *cis*-1,4-polybutadiene vulcanized with tetramethylthiuram disulfide (TMTD) by proton NMRI. Results are presented that demonstrate the ability of ^{1}H NMRI to spatially distinguish structural features of cured PB samples. Specifically, single- and multiple-echo (T_2-resolved) images are shown of samples whose cross-link densities were varied by changing either the length of cure time or the level of curing agent. In preparation for imaging, all samples in this study were extracted to remove nonnetwork material and then swollen with deuterated solvent. NMR images of the swollen materials have been obtained that therefore probe spatial variations in the proton signal intensity of the rubber samples directly, in contrast to the more popular method involving detection of signal from a protic swelling solvent.

Experimental Section

All elastomer samples were produced from Polysar Taktene 1202 high *cis*-1,4-polybutadiene, stated by the manufacturer to possess initial cis, trans, and vinyl isomer contents of 97%, 1.4%, and 1.6% and to have number-, weight-, and *z*-average molecular weights of 95 000, 366 000, and 977 000, respectively. The stocks were blended on a Brabender mixer and were formulated to contain on a per hundred grams rubber basis either 2 or 10 phr of TMTD as the curing agent, corresponding to active sulfur levels of 0.54 and 2.70 phr, respectively. In addition, 5 phr of zinc oxide was added to both mixtures as a complexing agent for the TMTD. An auxiliary fatty acid chelating agent for the ZnO was omitted in these formulations, in a deliberate attempt to produce spatial inhomogeneity in the resultant cross-linked networks of the cured samples. Samples were vulcanized either as 1.5-mm-thick sheets or as 7-mm-diameter cylinders on a hydraulic press at 150 °C and a nominal pressure of 2000 psi for various lengths of time and then quenched by immersion in a finely powdered bed of dry ice.

Following vulcanization, the samples were extracted with cyclohexane for 12 h in a Soxhlet extractor. This step was intended to remove dispersed and sol-phase materials that might have obscured observation of features in the gel phases of primary interest. In order to restrict the possibility of subsequent oxidation of these samples, they were stored swollen with solvent at 40 °F in a refrigerator. Prior to imaging, the cyclohexane was

---

* Author to whom correspondence should be addressed.

0024-9297/91/2224-3496$02.50/0

removed by vacuum. The samples were then transferred to NMR imaging tubes and reswollen by using fully deuterated cyclohexane.

Nominal cross-link densities were determined for all cured samples at ambient temperature by the equilibrium swelling method, using cyclohexane as the swelling solvent. Each sample's number-average molecular weight between physical cross-links, $M_{n,phys}$, was derived by use of the Flory-Rehner equation[21]

$$1/M_{n,phys} = \nu = \frac{-[\ln(1 - V_r) + V_r + \chi V_r^2]}{\rho_r V_0 (V_r^{1/3} - V_r/2)} \qquad (1)$$

in which ν represents the network chain density in moles of chains per gram of rubber, V_r is the volume fraction of rubber in the swollen vulcanizate, χ is the Huggins solvent-polymer interaction constant, ρ_r is the unswollen rubber density, taken to be 0.915 g/cm^3, and V_0 is the molar volume of the swelling solvent, taken as 108 cm^3/mol. On the basis of the results of previous work by Kraus, who studied swelling behavior in a similar polybutadiene system,[22] the value of the interaction parameter χ in eq 1 was evaluated for each sample as a linear function of V_r

$$\chi = 0.37 + 0.52 V_r \qquad (2)$$

Values of V_r were determined from the weight difference of the extracted samples compared, unswollen and swollen to equilibrium, namely

$$V_r = \left[\left(\frac{\rho_r}{\rho_s}\right) \left(\frac{W_s - W_u}{W_u}\right) + 1 \right]^{-1} \qquad (3)$$

where ρ_s is the solvent density, taken as 0.779 g/cm^3, W_s is the measured weight of the swollen rubber sample at equilibrium, and W_u is the measured weight of the unswollen sample.

All samples were imaged at ambient temperature on a Bruker MSL300 spectrometer (proton frequency of 300.13 MHz). The samples were contained in either 8.5- or 14.5-mm-i.d. glass tubes and were positioned vertically in the instrument's microimaging probe, which was equipped with a saddle-type radio-frequency coil of either 15- or 25-mm diameter. The images were obtained by a standard CPMG spin-echo (selective 90°/phase-shifted, nonselective 180°) pulse cycle,[23] with collection of either a single or eight sequential echoes. Schematic diagrams of the two imaging schemes are shown in Figure 1A,B. Slice-select, readout, and phase-encoding gradients were applied perpendicular to, and in the horizontal and vertical directions of, the images, respectively. In all cases, the excitation pulse shape was Gaussian of 1-ms duration, and the slice-select gradient strength was adjusted to maintain a nominal slice thickness of 1 mm. The readout and phase-select gradient strengths were tailored to suitably expand the images and to obtain square pixel dimensions. Delays in the pulse sequences were set to acquire images using echo times within a range determined by the longest T_2 observed for the uncured rubber. Specific values of these and other pertinent acquisition parameters are enumerated in the following section as part of the discussion of each sample's image.

Results and Discussion

Single-echo images are shown in Figure 2A-C of three extracted cylindrical PB samples, swollen with deuterated cyclohexane to a constant diameter of 8.5 mm. All three images were acquired using the pulse sequence illustrated in Figure 1A. The samples are distinguished by having been cured to different cross-link densities. The sample in Figure 2A was made from the formulation containing 2 phr of TMTD by curing at 150 °C for 60 min. The samples of Figure 2B,C, on the other hand, were cured at 150 °C from the mixture containing 10 phr of TMTD for periods of 5 and 60 min. On the basis of the results of equilibrium swelling measurements, the three extracted samples were characterized as having $M_{n,phys}$ values of 19 500, 8270, and 5720, corresponding to average numbers of monomer units between cross-link or entanglement sites of 361, 153, and 106, respectively.

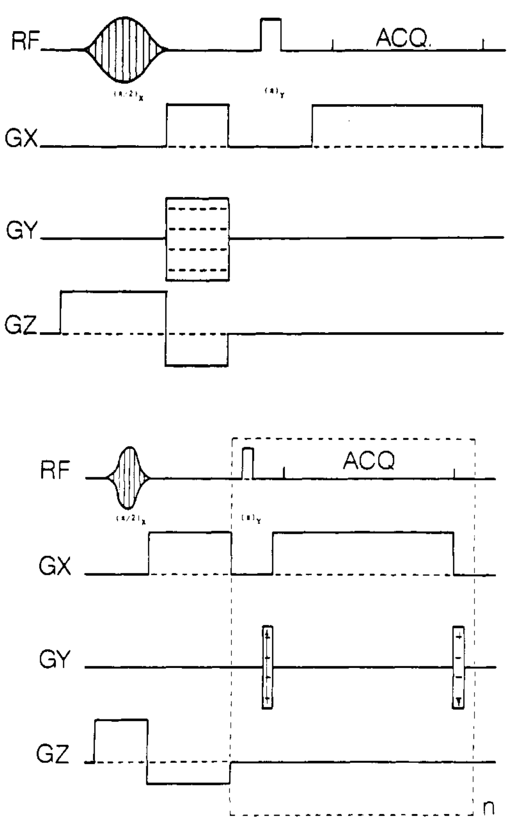

Figure 1. Imaging pulse sequences used in this study: (A) single-echo CPMG spin-echo pulse sequence, using selective 90° excitation/nonselective 180° refocusing radio-frequency pulses; (B) multiecho CPMG pulse sequence, using n repetitions of the refocusing hard pulses.

All three images were acquired by the 15-mm radio-frequency coil insert, with the readout gradient set at 15.45 G/cm and the phase-encode gradient varying between −7.73 and +7.73 G/cm, in 0.06 G/cm increments. Pulse repetition and echo times (TR and TE) were uniformly 5 s and 6.00 ms. The carrier frequency was centered in all three cases at 4.0 ppm, midway between the resonant frequencies of the methylene and methine protons of PB at 2.0 and 5.3 ppm. Thirty-six scans per phase-encode step were signal-averaged in producing each image, using 90°-increment ($X, -Y, -X, Y$) phase cycling. Combination of this number of scans with the setting of the receiver gain, which was repeatedly adjusted for each sample to optimize echo signal intensity, resulted in average signal-to-noise ratios of 11.0, 4.92, and 3.12 for images A-C in Figure 2, respectively. Given the spectral width of 62 500 Hz used in acquisition of each phase-encoded profile, the field-of-view (FOV) of these images is 9.5 mm × 9.5 mm, displayed as 256 × 256 pixels. Hence, the effective "pixel" resolution of the three images is 37 μm/pixel. Finally, the intensity scale of each image was optimized to highlight the contrast of features among the three samples.

Morphological features are evident in these images, indicative of large structural inhomogeneities within the samples. Consistent with macroscopic observation, for instance, the semicircular void at the edge of the image in Figure 2A resulted from an air bubble that became trapped at the wall of the sample tube. Similar circular voids within this image may likewise be interpreted as originating from entrainment of air in the sample on being swollen, although they may also be the result of recession of the rubber from the sites of true defects, such as areas of low cross-link density or agglomerates of ZnO. Another example of a clearly distinguishable inhomogeneity known to exist from macroscopic observation is seen in the image

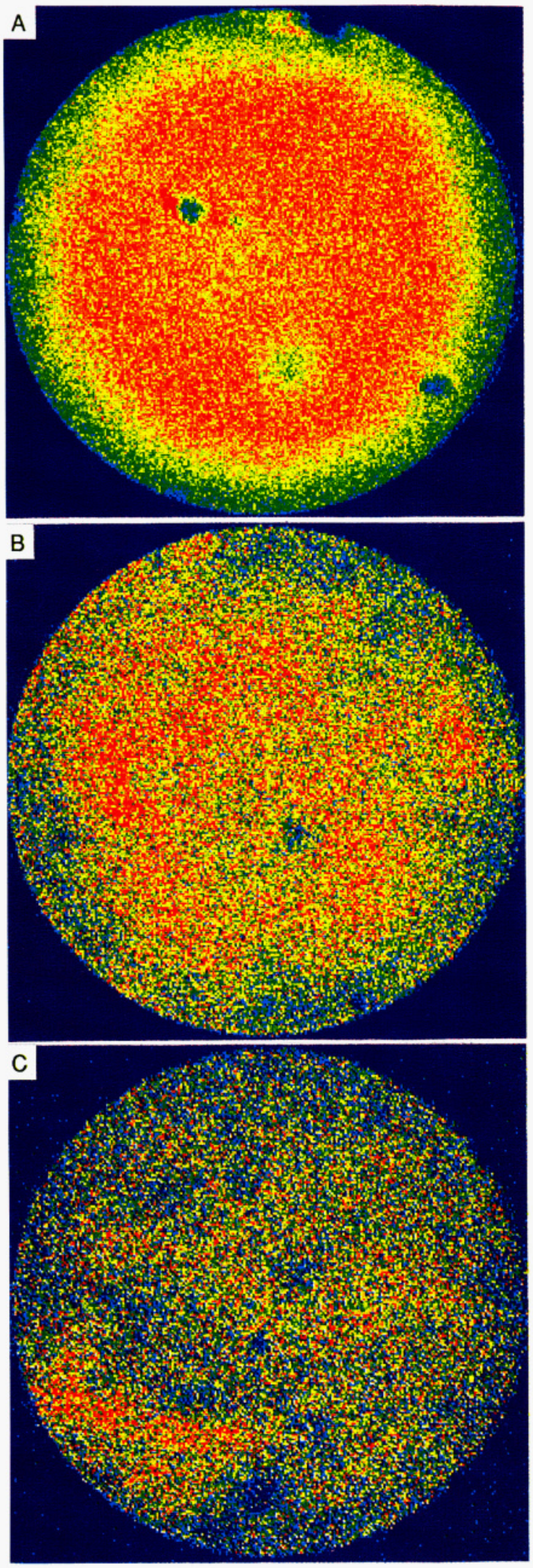

Figure 2. (A) Single-echo image of PB disk cured with 2 phr of TMTD for 60 min at 150 °C. FOV = 19 mm × 19 mm, displayed as 256 × 256 pixels. S/N = 11.0. (B) Single-echo image of PB disk cured with 10 phr of TMTD for 5 min at 150 °C. FOV = 19 mm × 19 mm, displayed as 256 × 256 pixels. S/N = 4.92. (C) Single-echo image of PB disk cured with 10 phr of TMTD for 60 min at 150 °C. FOV = 19 mm × 19 mm, displayed as 256 × 256 pixels. S/N = 3.12.

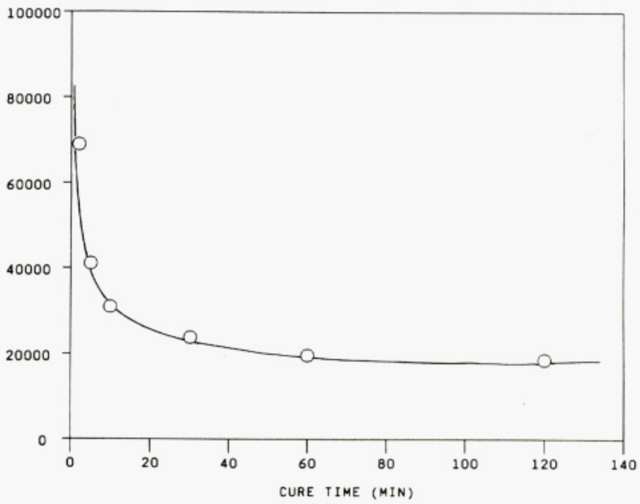

Figure 3. Experimental $M_{\mathrm{n,phys}}$ versus cure time at 150 °C for a mixture cured using 2 phr of TMTD.

in Figure 2C, whose arc-shaped region of high signal intensity toward the lower left coincides with a crack that developed on swelling this sample.

More general differences in signal intensity among the samples must be explained in terms of similar variations in the relaxation parameters characterizing the structure of the materials. It has been shown[24] that, given appropriate imaging conditions, the observed signal intensity, S, may be modeled by the simple expression

$$S = \rho^* \exp\{-\mathrm{TE}/T_2\}\{1 - \exp(-\mathrm{TR}/T_1)\} \qquad (4)$$

Further simplification of this expression is possible in the present case if it is assumed that, following the physical density of the materials, the signal density ρ is reasonably constant among the three samples as a result of being constrained to the same dimensions and that T_1 weighting of these images is either negligible given the value of TR used or unobservable at the present scale of magnification. Taken together, these assumptions imply that the variations of signal intensity displayed in these images are largely attributable to T_2 weighting. This interpretation is consistent with the results of previous investigatioins of the relative dependence of T_1 and T_2 values on the density of cross-linking and molecular entanglements in cross-linked elastomer networks.[25-30] Specifically, these studies have shown that the behavior of T_2 at temperatures well above T_g, as is the case here, is a sensitive indicator of variations in the low-frequency, long-range cooperative motions of chain segments between nodal junctures of such networks.

Accepting then the premise that, with the exception of voids, the T_2-weighted signal intensity of each pixel serves to characterize the degree of segmental motion of its contents, distribution of signal intensity among these three images is readily explained. For example, the decline in the S/N ratio of the images with increasing cure demonstrates that, as the average length of chain segments between effective cross-link sites decreases, so does the extent of their relative motion. One would similarly expect diminished T_2 values to typify constrained molecular motions brought about by restricting the samples to smaller than equilibrium dimensions. Thus, the low-intensity periphery of the sample in the image in Figure 2A may be viewed as the result of either of higher cross-link density in this region than in the interior of the sample, due to a thermally induced reaction gradient, or of a higher local degree of motional anisotropy in this area due to compression of the sample against the wall of the sample tube.

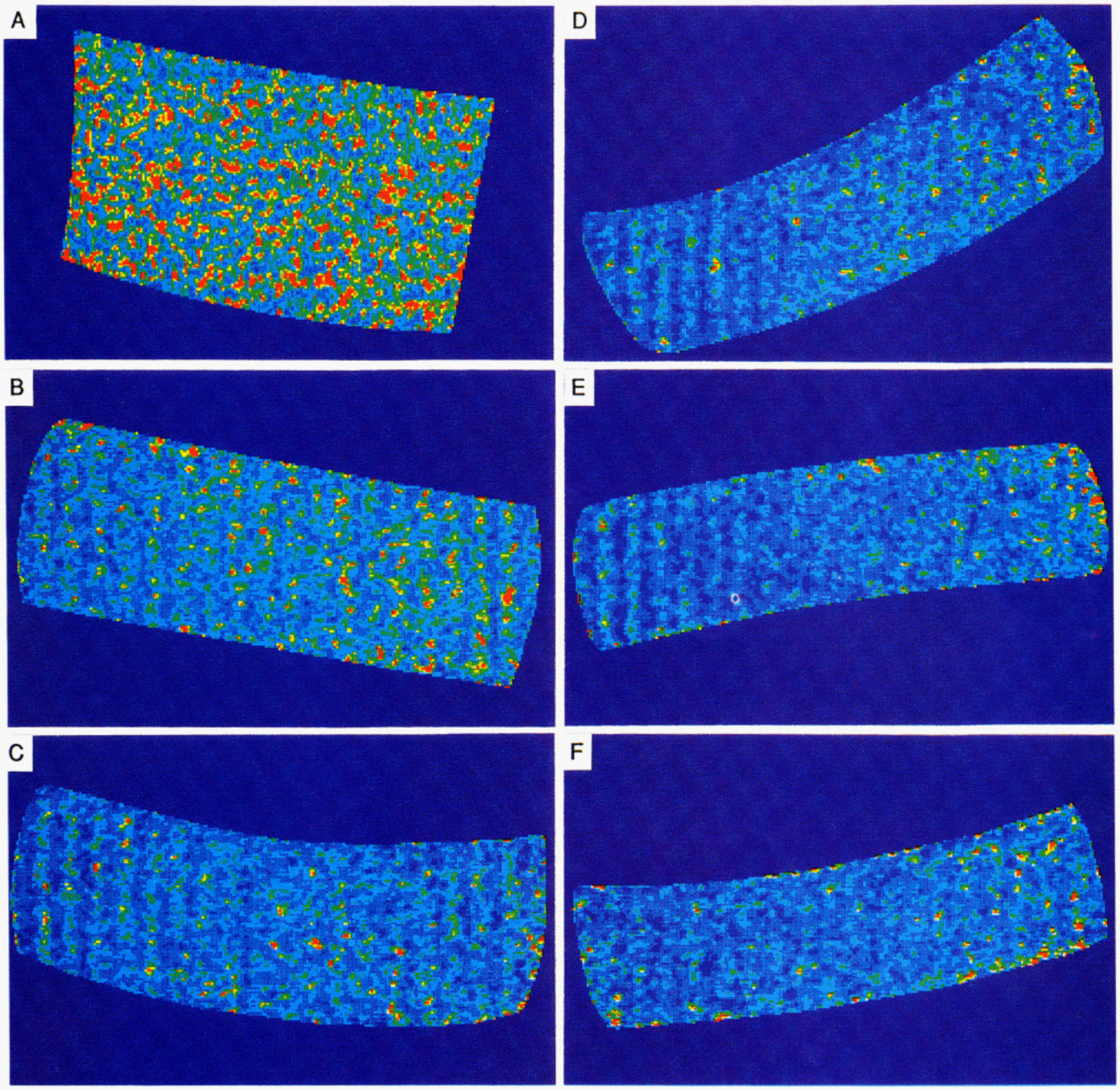

Figure 4. (A) T_2-resolved multiecho image of swollen PB sample, cured with 2 phr of TMTD at 150 °C for 2 min. FOV = 14.9 mm × 14.9 mm, displayed as 256 × 256 pixels. (B) T_2-resolved image of swollen PB sample cured with 2 phr of TMTD at 150 °C for 5 min. FOV = 14.9 mm × 14.9 mm, displayed as 256 × 256 pixels. (C) T_2-resolved image of swollen PB sample cured with 2 phr of TMTD at 150 °C for 10 min. FOV = 14.9 mm × 14.9 mm, displayed as 256 × 256 pixels. (D) T_2-resolved image of swollen PB sample cured with 2 phr of TMTD at 150 °C for 30 min. FOV = 14.9 mm × 14.9 mm, displayed as 256 × 256 pixels. (E) T_2-resolved image of swollen PB sample cured with 2 phr of TMTD at 150 °C for 1 h. FOV = 14.9 mm × 14.9 mm, displayed as 256 × 256 pixels. (F) T_2-resolved image of swollen PB sample cured with 2 phr of TMTD at 150 °C for 2 h. FOV = 14.9 mm × 14.9 mm, displayed as 256 × 256 pixels.

Contributions from both these effects is, of course, also possible. The existence of concentration-dependent cross-link density gradients is suggested in the images in Figure 2B,C by their angularly nonsymmetrical distributions of signal intensity, presumably the result of nonuniform mixing. Finally, the higher signal intensity observed in the vicinity of the crack in the image in Figure 2B is attributed to the less hindered motions of scissioned chain segments in this region.

In an attempt to more systematically investigate the dependence of T_2 values on cross-link density, a series of six samples were prepared from the vulcanization mixture containing 2 phr of TMTD. These samples were cured as thin sheets rather than as cylinders, on the assumption that spatial inhomogeneities in cross-link density produced by thermal gradients would be correspondingly diminished. The samples were cured for periods of 2, 5, 10, and 30 min and 1 and 2 h and were determined following extraction to have $M_{n,phys}$ values of 69 200, 41 200, 31 100, 23 900, 19 800, and 18 700, respectively. These results are shown plotted in Figure 3 and correspond to values expressed as the average number of monomer units between cross-link points of 1280, 762, 575, 442, 366, and 346. Appropriately sized portions of the extracted sheets were swollen to equilibrium dimensions inside 14.5-mm imaging tubes using C_6D_{12}.

Multiecho images of these samples were acquired by using the 25-mm probe insert and the pulse sequence illustrated in Figure 1B. The readout gradient strength was 9.85 G/cm, and the phase-encoding gradient strength varied between −4.93 and +4.93 G/cm in 256 equal increments. In this series, the pulse repetition times was 6 s, the echo times were eight sequential multiples of 8.05 ms, and the carrier frequency was again centered between the $-CH_2$ and $=CH$ proton resonances for PB. Four scans per phase-encoding step were signal-averaged using 90°-increment phase cycling, and the receiver gain was held constant for all six images in order to maintain uniform scaling. From sample to sample in the series, a small amount of reshimming was required to accommodate slight differences in size, shape, and orientation of the samples in the probe.

Sequential single-echo images produced for each of the six samples were processed to create the T_2 images shown in Figure 4A–F. Manipulation of the raw data consisted of pixel-by-pixel nearest-neighbor averaging of the single-echo images, followed by their input to a weighted nonlinear least-squares optimization routine, which calculated best fit single-exponential decay T_2 parameters for each of the 256 × 256 pixels in the image array. These and other procedures alluded to in reference to image manipulation are subroutines of a resident computer software program and are described elsewhere in greater detail.[24]

On the observation of a regular pattern of alternating average signal intensity that persisted through all six sets of images derived from the multiecho pulse train, separate series of odd-echo (1st, 3rd, 5th, and 7th) and even-echo (2nd, 4th, 6th, and 8th) T_2-resolved images were generated and compared. Resolution of features was found to be qualitatively similar between the two sets of images. Characteristic parameters from both series are reported in Table I. However, T_2 values computed for the even-echo series of images are assumed to be more accurate, on grounds that the attenuating effect of 180° pulse imperfections is largely compensated in a CPMG pulse train on alternate echoes. The sample images displayed in Figure 4A–F are therefore T_2-resolved based on the rate of decay of signal intensity in their respective even-echo images. Furthermore, in contrast to the previous set of images, the intensity scale is uniform throughout this series, so that the images may be compared directly with one another. Maximum signal intensity, displayed as red, corresponds to a T_2 of 300 ms.

The effective resolution of the six images in this set, given their FOV of 14.9 mm × 14.9 mm, is 58 μm/pixel. Alternately expressed in frequency units, since the images were acquired by using a total spectral width of 62 500 Hz, each pixel in these images spans a frequency range of 244 Hz. To enable comparison of this pixel dimension with the line widths of the resonances being imaged, 90°-pulse FID spectra were recorded for each of the samples. The results are displayed as spectra in Figure 5 and as measured Lorentzian half-widths and derived T_2^* values in Table I. The main resonances seen in Figure 5 at 2.0 and 5.3 ppm represent the combined cis-1,4 and trans-1,4 signals of methylene and methine protons, respectively, while the shoulder peak at 1.3 ppm is attributable to vinyl methylene protons.[31] The methine protons of the vinyl groups are not resolved in these spectra. The half-width values reported in Table I confirm that neither of the two major resonances individually exceeded the effective pixel spectral width at any of the six cure times.

Unfortunately from the standpoint of obtaining unique T_2 information in each pixel, the presence of two intense resonances in the proton spectrum of PB introduces a chemical shift artifact to these images, negating the usual single-resonance line-width criterion for assessing image resolution. In fact, given the 990-Hz (3.3 ppm) chemical shift separation of these two resonances, carryover of signal intensity over a spatial dimension of about four pixels is observed in these images. A second type of artifact was additionally introduced to the T_2 images by the preliminary step of spatially averaging the single-echo images. The effect of this nearest-neighbor signal-averaging procedure applied to single-echo images already distorted by the existence of a chemical shift artifact leads to a general blurring of image resolution in the T_2-resolved images. Since the latter procedure was deemed necessary to compensate deterioration of T_2 image quality induced by poor S/N in the single-echo images collected at the longer echo times, it is assumed that its use in future imaging experiments will be avoidable by collecting a greater number of scans or by shortening the echo delays.

Disregarding momentarily the effect of artifacts in distorting the appearance of sample morphology in these images, attention is focused instead on the histograms that accompany the images, shown together in Figure 6. The histograms represent the imaging results as plots of the number of pixels with a particular T_2 versus T_2, and display a consistent trend toward narrower distributions centered at increasingly shorter T_2 values as the cure time, and hence, the cross-link density of the rubber, increases. A second distinguishing feature of the histograms is their skewed nature at all cure times, favoring the long T_2 range. These characteristics are expressed quantitatively in the data of Table I, which presents statistical parameters for the histograms analyzed as single-population distributions. Reported are the average, median, mode, and standard deviation T_2 values for each image as calculated from its histogram.

Interpretation of the T_2 distributions of these images to obtain information on the spatial variation in the cross-link density of the rubber samples as a function of cure, which is the primary objective of this study, requires that a model be assumed interrelating T_2 and ν. The simplest such model having reasonable theoretical justification in application to cross-linked elastomers characterizes the dynamic behavior of these networks in terms of two distinct populations of chain segment correlation times, τ_c.[28] The two τ_c populations are assumed to be distributed about long and short average correlation times, τ_{cL} and τ_{cS}, which have temperature dependences obeying the Arrhenius relationship. These average values of τ_c are associated, respectively, with motionally restrained regions of the elastomer network in the vicinity of chemical or physical cross-links and with relatively unrestrained chain segment regions statistically far removed from cross-link sites.

It is further assumed that the behavior of T_2 as a function of τ_c is adequately described by the BPP expression for homonuclear dipole–dipole relaxation by the mechanism of intramolecular rotational reorientation,[32] stated here as

$$\frac{1}{T_2} \propto 3\tau_c + \frac{5\tau_c}{1+\omega^2{\tau_c}^2} + \frac{2\tau_c}{1+4\omega^2{\tau_c}^2} \qquad (4)$$

where ω is the precessional frequency of the observed nucleus. Equation 4 shows that, in either of the limiting cases $\omega\tau \gg 1$ or $\omega\tau \ll 1$, T_2 is inversely proportional to τ_c. The assumption of long and short average values of τ_c in elastomer networks under these conditions is therefore taken to imply the existence of inversely related short and long values of the transverse relaxation parameter, T_{2S} and T_{2L}, which are similarly associated with cross-linked

Table I
T_2 Characteristics of PB Samples Cured with 2 phr of TMTD, Determined from Single $\pi/2$ Pulse Line-Width Measurements and from Spin-Echo T_2-Resolved Image Histograms

	sample cure time					
	2 min	5 min	10 min	30 min	60 min	120 min
line width, Hz						
$-CH_2$	31.8	48.0	55.6	68.1	64.5	53.0
$=CH$	30.2	47.9	54.5	67.4	70.6	47.1
T_2^*, ms						
$-CH_2$	10.0	6.6	5.7	4.7	4.9	5.8
$=CH$	10.5	6.6	5.8	4.7	4.5	5.3
T_2 mode, ms						
even echo	71.8	58.8	50.6	48.2	44.7	45.9
odd echo	45.9	41.2	38.8	31.8	30.6	29.4
T_2 average, ms						
even echo	130.1	85.0	68.5	63.1	61.9	64.7
odd echo	93.1	56.8	46.9	39.0	35.7	34.1
T_2 median, ms						
even echo	178.6	112.5	88.0	81.5	83.9	90.3
odd echo	153.3	76.0	56.7	46.1	41.0	41.2
std dev, ms						
even echo	79.4	48.3	36.6	34.1	36.8	40.7
odd echo	74.9	33.0	21.5	16.7	13.9	15.6

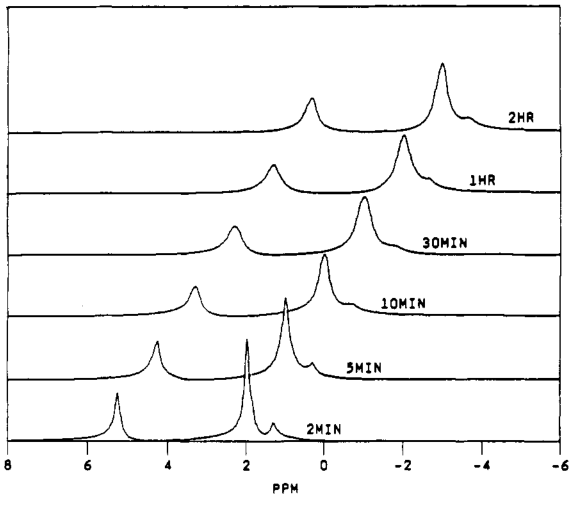

Figure 5. Single 90°-pulse FID spectra of the samples shown imaged in Figure 4A–F. All resonance assignments are given in the text.

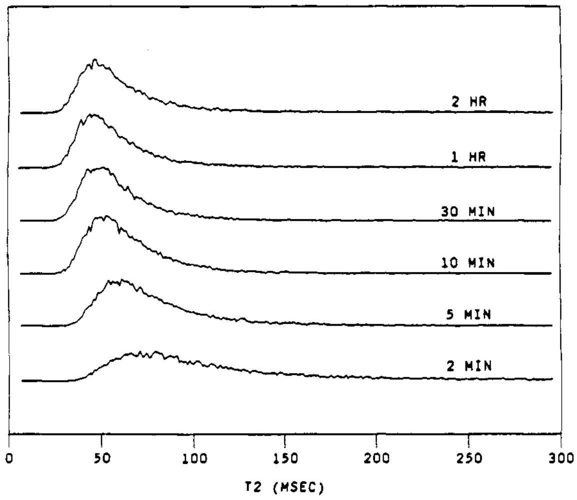

Figure 6. Histograms of the number of pixels with a particular T_2 versus T_2 value for the six sample images presented in Figure 4A–F. Statistical parameters derived from these are given in Table I.

and uncross-linked regions of the samples.

Extension of this approach to the present task of determining cross-link density distributions from experimentally observed T_2 distributions suggests modeling each T_2 component of the image histograms as a volume fraction weighted inverse average of short and long values of the relaxation parameter, namely

$$\frac{1}{T_{2i}} = \frac{V_{xi}}{T_{2S}} + \frac{(1 - V_{xi})}{T_{2L}} \tag{5}$$

where V_{xi} is the volume fraction of the material per pixel associated with T_{2S}, characteristic of the cross-linked regions, and $1 - V_{xi}$ is the volume fraction per pixel of the remaining nonsolvent material associated with T_{2L}. The averaging procedure indicated by eq 5 ignores any contribution to the observed T_2 distributions made by the volume fraction of deuterated solvent contained within each sample. Equivalently stated, the T_2 of the solvent fraction, characterizing randomly fluctuating noise, is implicitly taken to be infinite.

The significance of the V_{xi} in this model is that they are considered to be proportional to the volumetric chain density per pixel, ν_i, by the scaling factor α, representing half the mass of polymer repeat units per cross-link region. Equation 5 may thus be expressed as

$$\frac{1}{T_{2i}} = \frac{\alpha\nu_i}{T_{2S}} + \frac{(1 - \alpha\nu_i)}{T_{2L}} \tag{6}$$

which may be rearranged to the form

$$\frac{1}{T_{2i}} = [\alpha(T_{2S}^{-1} - T_{2L}^{-1})]\nu_i + T_{2L}^{-1} \tag{7}$$

If the pixel quantities ν_i are assumed to spatially average to the bulk sample cross-link densities measured by equilibrium swelling, the slope and intercept of eq 7 are obtainable as least-squares parameters of straight-line fits to plots of $(1/T_{2i})_{av}$ versus $\nu_{swelling}$, where $(1/T_{2i})_{av}$ is computed from the $1/T_{2i}$ by using normalized histogram frequencies as weighting coefficients. Finally, given these parameters of the model, ν_i distributions for the various samples are calculable from their respective T_{2i} distributions by substitution into the inverted form of eq 7

$$\nu_i = \frac{(T_{2i}^{-1} - T_{2L}^{-1})}{[\alpha(T_{2S}^{-1} - T_{2L}^{-1})]} \tag{8}$$

This analysis of the data has been carried out. Plots of $(1/T_{2i})_{av}$ versus $\nu_{swelling}$ for both the even- and odd-echo generated images are illustrated graphically in Figure 7. The results of the odd-echo series are seen to conform well

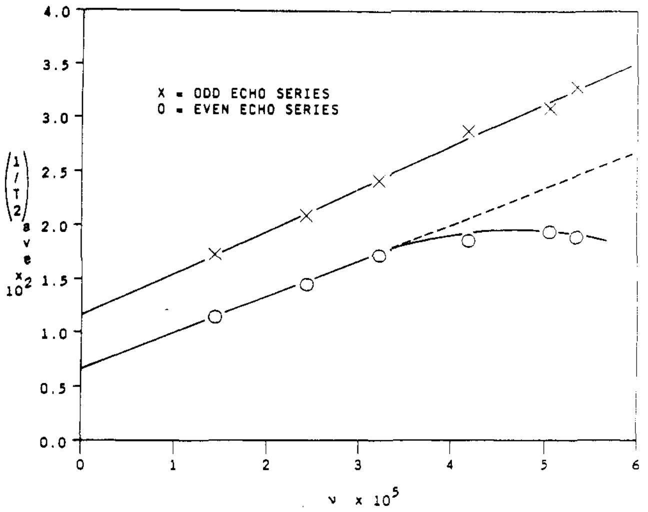

Figure 7. Plots of the $(1/T_{2i})_{\mathrm{av}}$ versus ν_{swelling} for the even- and odd-echo series of T_2-resolved images.

to the linear behavior predicted by eq 7, whereas the data from the even-echo series demonstrate negative deviations, increasing with cure time, from an initial linear trend. In an attempt to account for this negative curvature of the even-echo data, two intuitively motivated empirical modifications to the basic theoretical model were evaluated.

Consideration was given first to the possibility that, since the characteristic time scales for T_2 relaxation and equilibrium swelling behavior are vastly different, the T_2 averages might preferentially reflect each sample's concentration of covalently bonded chemical cross-link structures, whereas it is known that the measured ν values reflect contributions from both chemical cross-links and permanently entrapped physical entanglements. On this basis, the ν values were extrapolated to their respective chemical cross-link densities using the proposed correction schemes both of Moore and Watson[33] and of Kraus[22] and replotted against $(1/T_{2i})_{\mathrm{av}}$. This modification produced slight increases in the slopes and corresponding decreases in the intercepts of the best straight lines through the experimental data. However, due to the quadratic form of the transformation of the ν scale effected by both correction schemes, the curvature of the even-echo series data was actually enhanced.

Second, in an effort to take into account a previously unassumed explicit dependence of the measured T_2 distributions on the decreasing equilibrium dimensions of the swollen samples with increasing cross-link density (or equivalently, on the increasing volume fraction of rubber per pixel), the data were replotted as $V_{\mathrm{r}}(1/T_{2i})_{\mathrm{av}}$ versus ν. This procedure was suggested by the following modified version of eq 5

$$\frac{1}{T_{2i}} = \frac{V_{xi}/V_{\mathrm{r}}}{T_{2\mathrm{S}}} + \frac{(1 - V_{xi})/V_{\mathrm{r}}}{T_{2\mathrm{L}}} \tag{9}$$

and successfully yielded plots for both sets of data of significantly increased linearity. However, the intercepts of these plots implied physically meaningless large, negative values for $T_{2\mathrm{L}}$. Substitution of entanglement-corrected values of ν into eq 9 produced similar results.

No simple explanation is advanced at present to account for the negative curvature of the even-echo data. The behavior mathematically reflects the tendency of the even-echo T_2 distributions to narrow more slowly than the rate of increase in ν for samples cured longer than 10 min. Physically, this may be a result of reversion processes occurring in these samples that are more sensitively reflected by T_2 than by equilibrium swelling, such as a reduction in the average sulfur rank of the cross-links. A situation can be envisioned, for example, in which a number of clustered di- or polysulfidic cross-links react further to form a larger number of more widely spaced monosulfidic cross-links. On average, therefore, more mechanically effective chains could be formed, while at the same time increasing both the concentration of $T_{2\mathrm{S}}$ regions as well as the population of chain lengths characterized by $T_{2\mathrm{L}}$. The result of this sequence of events could account for the observed tendencies in the experimental data, ranging from inhibition of the decline in $(1/T_{2i})_{\mathrm{av}}$ to an actual regrowth of its value. This line of reasoning seems especially convincing in explanation of the behavior of the sample cured for 2 h, whose polydispersity assessed both by T_2 and by T_2^* actually exceeds that of the sample cured for 1 h.

From a more general standpoint, the issue of oversimplification in the underlying assumptions of the present model must be considered. It is possible, for instance, that the spatial averaging procedure assumed to correlate $(1/T_{2i})_{\mathrm{av}}$ with ν_{swelling} is not scale invariant. Questionable as well is the assertion that the T_2 distributions of these images can be accounted for by only two average values of τ_{c}. That τ_{cL}, at least, is not explicitly a function of either ν or V_{r} is clearly indefensible in light of direct evidence in the histograms of a consistent decline in $T_{2\mathrm{S}}$ with increasing ν. The constancy of τ_{cS}, and, hence, of $T_{2\mathrm{L}}$, is similarly doubtful on grounds that, even in an elastomer at a temperature well above its T_{g}, the frequency of transient intermolecular entanglements, which act to provide additional sources of T_2 relaxation, should increase with increasing V_{r}.

Previously cited studies of the temperature and molecular weight dependence of NMR relaxation parameters, in both poly(dimethylsiloxane)[25] and polybutadiene[28] elastomers, have conceded the inability to accurately model T_1 and T_2 behavior over full ranges of the independent variables without assuming a more complex distribution of molecular correlation times than is proposed in the present model. The work of these researchers was moreover conducted on bulk, unswollen materials. By comparison, the experimental conditions used in this study, while enabling characterization of the average mechanical properties of the sample networks, must be regarded as contributing yet another order of complexity to the interpretation of the T_2 results. Equivalently stated, the simple model employed in this study is more likely applicable to analyzing T_2 as a function of ν under conditions of roughly equal sample density than under conditions of equilibrium swelling, since in the former case the effect of variable V_{r} does not need to be considered.

In spite of these possible theoretical shortcomings, it does not seem intuitively likely that any systematic revision of the assumed model capable of predicting nonlinear behavior in the even-echo results would simultaneously anticipate the near perfect linearity of the odd-echo results. Considering as well the similarity found between the slope of the line through the first three data points of the even-echo series and that of the line through the entire data set of the odd-echo series, it is justifiable on at least a first approximation basis to complete analysis of the data according to this model in order to evaluate its full implications. Of particular interest are predictions for the dimensions of the effective cross-link regions and for the development in character of the cross-link density distributions with increasing cure time. The former quantity is desirable from the standpoint of interpreting

Table II
Characteristic Model-Related Cross-Link Density Parameters Obtained for T_2-Imaged PB Samples Cured with 2 phr of TMTD

	sample cure time					
	2 min	5 min	10 min	30 min	60 min	120 min
T_{2S}, ms						
even echo	30.6	25.9	22.4	21.2	20.0	20.0
odd echo	13.5	11.2	9.4	8.2	7.1	7.1
T_{2L}, ms						
even echo	153	153	153	(153)	(153)	(153)
odd echo	86.2	86.2	86.2	86.2	86.2	86.2
$\langle V_{xi} \rangle$						
even echo	0.184	0.247	0.280	(0.295)	(0.295)	(0.284)
odd echo	0.091	0.119	0.132	0.154	0.149	0.164
⟨RU⟩/network chain	1280	762	575	442	366	346
⟨RU⟩/xlink region						
even echo	470	376	322	(261)	(216)	(196)
odd echo	234	184	152	136	109	113
⟨Vol⟩/xlink region, $\mu m^3 \times 10^7$						
even echo	6.88	4.01	2.84	(2.00)	(1.46)	(1.30)
odd echo	3.42	1.94	1.36	1.04	0.74	0.75
$\nu_{swelling}$, mol/g × 10^5	1.45	2.43	3.22	4.19	5.06	5.35
$\langle \nu_i \rangle$, mol/g × 10^5						
even echo	1.66	2.47	3.27	(3.68)	(3.92)	(3.79)
odd echo	1.70	2.45	3.22	4.36	4.91	5.41

the capability of the imaging method to resolve spatial variations in cross-link density within a bulk elastomer sample, whereas the cross-link density distributions are useful for providing at least a general qualitative view of the progress of cross-linking events as vulcanization proceeds.

To continue then with this analysis of the results, observed values of T_{2S} and least-squares-derived values of T_{2L} and V_x are reported in Table II. Also tabulated are the number of PB repeat units per number-average network chain, obtained from the swelling measurements. Following these are values for the number of PB repeat units per cross-link region, calculated as twice the product of RU/network chain and V_x. Finally, effective volumes occupied by the cross-link regions have been calculated from the relationship

$$\text{vol/xlink region } (\mu m^3) = \frac{2V_x}{\nu \rho_r V_r N_A} \times 10^{12} \qquad (10)$$

where N_A is Avogadro's number. All derived values represent bulk averages for a given sample. The use of parentheses enclosing even-echo series results reported for the samples cured for 30 min and 1 and 2 h indicates that these were calculated on the basis of the slope and intercept of the best straight line through the previous three data points in this series.

Owing to their derivation from V_x, the number of RUs/cross-link region is predicted to decrease with increasing cure. This result could potentially be explained by the mechanism proposed earlier, involving reversion in the average sulfur rank of cross-links. However, to the extent the opposing argument regarding a suspected but unaccounted for dependence of T_{2L} on V_r is valid, V_x is progressively underestimated from its true value. The decline in the RUs/cross-link region values is therefore assumed more likely to reflect the need to take account of the influence of variable V_r in the present model rather than a tendency of the cross-link regions to encompass consistently less material as the degree of cross-linking increases. Although credible to some extent on grounds that the PB chains are less extended as V_r increases, the predicted reduction in the volume/cross-link region with increasing cure is similarly assumed to be overestimated.

It is nevertheless evident from the general trend in the values of V_x that average pixels in these images contain a significant fraction of PB chains characterized by T_{2S} and that this fraction increases with cure in a regular manner. Furthermore, given the fact that each pixel in these images represents a volume of ~3 × 10^6 μm^3, the values for the volume/cross-link region imply the number of cross-links within an average pixel to be on the order of ~10^{12}–10^{13}. Clearly, then, individual cross-links are not being detected in these images, even though the volumes within which they exert a measurable effect on T_{2i} contain on the order of ~10^2 monomer repeat units. This conclusion remains valid despite chemical shift and noise distortions of the images, so long as these distortions do not substantially alter the $1/T_{2i}$ averages of the histograms.

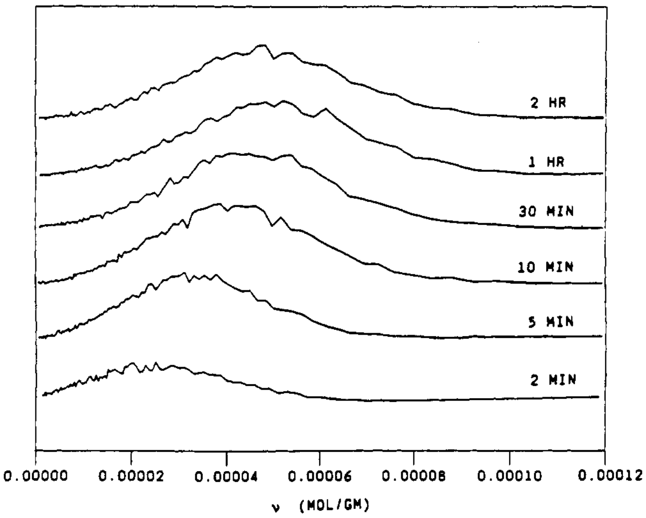

Figure 8. Histograms of ν values computed by using least-squares parameters obtained from the even-echo T_2 image series.

As a final interpretation of the experimental results by the present model, distributions of ν_i may be obtained from the T_{2i} distributions using eq 8. Histograms of the computed ν_i based on the least-squares parameters of the even-echo T_2 image series are shown in Figure 8. These display anticipated similarities to the T_2 histograms. Although the nonlinear transformation of scale in converting T_{2i} to ν_i results in closer spacing of consecutive points in the ν_i histograms at low ν than at high ν, the general tendencies of the distributions to narrow and to be centered at higher average values of ν parallel the trends of the T_2 histograms.

Through inspection of the ν_i averages reported in the bottom three rows of Table II, a growing discrepancy between calculated and measured averages of ν is observed for the even-echo series results beyond 10 min of cure time, following the behavior of the $1/T_{2i}$ averages. That the calculated ν_i averages are otherwise generally greater than their measured counterparts is a consequence of excluding from the calculated averages any negative values of ν_i. The latter result mathematically from eq 8 whenever T_{2i} is greater than T_{2L}. Again, it is expected that both sources of disagreement between these two sets of values for the average cross-link densities of the samples would be minimized or eliminated by properly accounting for the dependence of T_{2L} on V_r.

Conclusions

The results of this study demonstrate the ability of ^{1}H NMRI to spatially resolve a variety of structural features in unfilled, swollen samples of TMTD-vulcanized *cis*-polybutadiene. By use of deuterated cyclohexane as the swelling solvent, direct proton images of the rubber networks have been obtained. Large-scale inhomogeneities, such as voids and defects, have been shown to be observable by visual inspection of T_2-weighted single-echo images. Gradients in signal intensity within these images, related either to a higher degree of cure at the mold/rubber interface or to compression of the samples, have also been noted.

While rendered less distinct by the existence of chemical shift and signal-averaging artifacts, evidence of spatial variation in the distribution of effective cross-link structures within progressively cured samples has been shown to exist in histograms of their T_2-resolved multiecho images. Analysis of the histograms implies that cross-links exert a discernible effect on T_2 over volumetric dimensions of $\sim 10^{-7}\ \mu\text{m}^3$ and that the concentration and spatial dispersion of cross-link structures change with increasing cure in an overall predictable fashion. Among possible sources of deviation from the linear correlation between inverse T_2 averages and equilibrium swelling determined cross-link density averages predicted by the model used to interpret the T_2 distributions, reversion effects and failure to properly assess the influence of the variable extension of the swollen samples on T_2 have been considered.

Clearly, more rigorous treatments of the relationships between cross-link density, chain extension, and NMR relaxation parameters remain to be evaluated. The analysis of data collected from chemical shift deconvoluted T_2 images is also warranted, as a means of validating the parameters derived from the present set of images. However, the basic approach outlined in this article provides an alternative method for characterizing the progress of vulcanization events in polybutadiene. The results that have been obtained can be taken to complement the findings of one-dimensional NMR spectroscopic studies of the process. Logical extensions of NMR imaging techniques should prove equally applicable to investigating the development of network structure in other cross-linked elastomer systems. Correlations found between the two- and three-dimensional structural characteristics of cross-linked elastomers and their transient mechanical behavior should ultimately enable prediction of the performance characteristics of these materials based on knowledge of their molecular architecture.

Acknowledgment. We thank Polysar, Ltd., for their contribution of the formulated Taktene 1202 samples used in this study.

References and Notes

(1) Bovey, F. A. *High Resolution NMR of Macromolecules*; Academic Press: New York, 1972.
(2) *High Resolution NMR Spectroscopy of Synthetic Polymers in Bulk*; Komoroski, R. A., Ed.; VCH Publishers: Deerfield Beach, FL, 1986.
(3) Andreis, M.; Koenig, J. L. *Adv. Polym. Sci.* **1989**, *89*, 69.
(4) Mullins, L.; Thomas, A. G. In Theory of Rubber-Like Elasticity. *The Chemistry and Physics of Rubber-Like Substances*; Bateman, L., Ed.; Maclaren: London, 1963; Chapter 7.
(5) Saville, B.; Watson, A. A. *Rubber Chem. Technol.* **1967**, *40*, 100.
(6) Queslel, J.; Mark, J. E. In Mechanical and Solvent-Swelling Methods for Characterizing Insoluble Polymer. *Determination of Molecular Weight*; Cooper, A. R., Ed.; John Wiley and Sons: New York, 1989; Chapter 16.
(7) Mansfield, P.; Grannell, P. K. *Phys. Rev. B* **1975**, *12*, 3618.
(8) Wind, R. A.; Yannoni, C. S. *J. Magn. Reson.* **1979**, *36*, 269.
(9) Szeverenyi, N. H.; Maciel, G. *J. Magn. Reson.* **1984**, *60*, 460.
(10) Emid, J.; Creyghton, J. H. N. *Phys. B+C (Amsterdam)* **1985**, *128B+C*, 81.
(11) Chou, M. H.; Lee, C. J.; Shydind, D. N.; Weitekamp, D. P. *Phys. Rev. Lett.* **1985**, *55*, 1923.
(12) DeLuca, J.; Nuccetelli, C.; DeSimone, B. C.; Maraviglia, B. *J. Magn. Reson.* **1986**, *67*, 169.
(13) Suits, B. H.; White, D. *J. Appl. Phys.* **1986**, *60*, 3772.
(14) Chingas, G. C.; Miller, J. B.; Garroway, A. N. *J. Magn. Reson.* **1986**, *66*, 530.
(15) McDonald, P. J.; Attard, J. J.; Taylor, D. G. *J. Magn. Reson.* **1987**, *72*, 224.
(16) Cory, D. G.; van Os, J. W. M.; Veeman, W. S. *J. Magn. Reson.* **1988**, *76*, 543.
(17) Miller, J. B.; Garroway, A. N. *J. Magn. Reson.* **1988**, *77*, 187.
(18) Cory, D. G.; Veeman, W. S. *J. Magn. Reson.* **1989**, *82*, 374.
(19) Cory, D. G.; de Boer, J. C.; Veeman, W. S. *Macromolecules* **1989**, *22*, 1618.
(20) Chang, C.; Komoroski, R. A. *Macromolecules* **1989**, *22*, 600.
(21) Flory, P. J. *J. Chem. Phys.* **1950**, *18*, 108.
(22) Kraus, G. *J. Appl. Polym. Sci.* **1963**, *7*, 1257.
(23) Meiboom, S.; Gill, D. *Rev. Sci. Instrum.* **1958**, *29*, 688.
(24) Liu, J.; Nieminen, A. O. K.; Koenig, J. L. *J. Magn. Reson.* **1989**, *85*, 95.
(25) Charlesby, A.; Folland, R.; Steven, J. H. *Proc. R. Soc. London A* **1977**, *355*, 189.
(26) Folland, R.; Steven, J. H.; Charlesby, A. *J. Polym. Sci., Polym. Phys. Ed.* **1978**, *16*, 1041.
(27) Folland, R.; Charlesby, A. *Polymer* **1979**, *20*, 207.
(28) Rowland, T. J.; Labun, L. C. *Macromolecules* **1978**, *11*, 466.
(29) Munie, G. C.; Jonas, J.; Rowland, T. J. *J. Polym. Sci., Polym. Chem. Ed.* **1980**, *18*, 1061.
(30) Brown, D. R.; Munie, G. C.; Jonas, J. *J. Polym. Sci., Polym. Phys. Ed.* **1982**, *20*, 1659.
(31) Santee, E. R.; Chang, R.; Morton, M. *J. Polym. Sci., Polym. Lett. Ed.* **1973**, *11*, 449.
(32) Bloembergen, N.; Purcell, E. M.; Pound, R. V. *Phys. Rev.* **1948**, *73*, 679.
(33) Moore, C. G.; Watson, W. F. *J. Polym. Sci.* **1956**, *19*, 237.

Registry No. TMTD, 137-26-8.